

Two modes of sea-ice gravity drainage: A parameterization for large-scale modeling

Adrian K. Turner,¹ Elizabeth C. Hunke,¹ and Cecilia M. Bitz²

Received 21 August 2012; revised 6 March 2013; accepted 20 March 2013; published 7 May 2013.

[1] We present a new one-dimensional parameterization of gravity drainage implemented in an all-new thermodynamic component of the Los Alamos Sea Ice Model (CICE), based on mushy layer theory. We solve a set of coupled, nonlinear equations for sea-ice temperature (enthalpy) and salinity using an implicit Jacobian-free Newton-Krylov method. Time resolved observations of gravity drainage show two modes of desalination during growth. Rapid drainage occurs in a thin region just above the ice/ocean interface, while slower drainage occurs throughout the ice. Parameterizations are designed to represent each of these modes and work simultaneously. Near the interface, desalination occurs primarily via the fast drainage, while slow drainage continues to desalinate ice above the interface. The rapid desalination is convectively driven and is parameterized based on a consideration of flow driven upward within the mush and downward in chimneys, modified by the Rayleigh number. The slow desalination is represented as a simple relaxation of bulk salinity to a value based on a critical porosity for sea-ice permeability. It is shown that these parameterizations can adequately reproduce observational data from laboratory experiments and field measurements.

Citation: Turner, A. K., E. C. Hunke, and C. M. Bitz (2013), Two modes of sea-ice gravity drainage: A parameterization for large-scale modeling, *J. Geophys. Res. Oceans*, 118, 2279–2294, doi:10.1002/jgrc.20171.

1. Introduction

[2] Sea ice, the frozen surface of high latitude seas, is not entirely fresh but is composed of pockets and networks of brine surrounded by fresh ice. The brine is not fixed in the sea ice; brine inclusions expand and contract as the temperature of the ice changes and the fresh ice surrounding the brine network melts and refreezes. Channels form within the ice-brine material, through which a number of processes move the brine around and change the properties of the sea ice. The brine also harbors a rich variety of living organisms whose existence in the ice is enabled by the transport of nutrients into the ice with seawater through the brine network.

[3] The vertical salinity profile of sea ice changes shape during the first year, from a “C” shape with higher salinities at the top and the bottom than in the interior, to a profile characteristic of multiyear ice, with much fresher ice near the top surface and less salt content overall. The salinity structure of the ice impacts directly on heat conduction, melt/freezing rates and strength, and indirectly through the effect of the

sea-ice biology (changing albedo for example). As the seasonal ice fraction of the Arctic ice pack increases [Maslanik *et al.*, 2007; Comiso, 2012], the representation of the early evolution of the sea-ice salinity profile becomes more important in models. In the Southern Hemisphere, where the pack ice already is largely seasonal, such a representation will improve simulations of global and regional climate.

[4] The goal of this paper is to develop a sea-ice model with prognostic salinity for global climate modeling, in which horizontal grid scales are typically greater than 1 km. The microstructure and subgrid-scale heterogeneity of the ice cannot be explicitly modeled at such scales while remaining computationally tractable. We develop a vertical one-dimensional parameterization meant to represent the relevant processes without accounting for details of the microphysics.

[5] Recent work using mushy layer theory [Notz and Worster, 2009] has shown that all the salt in freezing seawater is initially incorporated into the ice-brine structure and that sea ice desalinates after formation. Two main processes desalinate sea ice. The first process is gravity drainage [Untersteiner, 1968], which is the draining of brine from sea ice by convection caused by an unstable brine density profile. This unstable profile is generated by the temperature profile present in forming sea ice. The second process is flushing, which occurs when temperatures rise and the upper surface of the ice and snow start melting. This generates melt water that can percolate through the sea ice and replace the salty brine by flushing it out to the ocean, thus lowering the bulk salinity. While flushing is also driven gravitationally

¹T-3 Fluid Dynamics and Solid Mechanics Group, Theoretical Division, Los Alamos National Laboratory, Los Alamos, New Mexico, USA.

²Department of Atmospheric Sciences, University of Washington, Seattle, Washington, USA.

Corresponding author: A. K. Turner, T-3 Fluid Dynamics and Solid Mechanics Group, Theoretical Division, Los Alamos National Laboratory, Mail Stop B210, Los Alamos, NM 87545, USA. (akt@lanl.gov)

©2013. American Geophysical Union. All Rights Reserved.
2169-9275/13/10.1002/jgrc.20171

it is not referred to as gravity drainage. In this paper we concentrate on gravity drainage, because flushing models already exist [e.g., *Vancoppenolle et al.*, 2007; *Jeffery et al.*, 2011]. Both gravity drainage and flushing depend critically on the vertical distribution of salinity and permeability in sea ice, but observations needed to guide and evaluate these process parameterizations are sparse.

[6] During sea-ice formation, the upper surface of the sea ice is colder than the base and a temperature gradient exists in the ice. In the colder, upper ice, the brine inclusions partially freeze, concentrating their brine and leading to an unstable density stratification. The brine undergoes convective overturning, with saltier brine being replaced with less salty ocean water. Downward flowing brine causes dissolution of the ice crystal matrix and the formation of brine channels through which downward flow is concentrated. Upward flow continues to be through mush [*Worster*, 1997]. This process has been studied for some time and has been modeled as mush Rayleigh convection, where convection occurs when the Rayleigh number of the ice-brine mush exceeds some critical value [*Worster*, 1992a]. This critical value will typically depend on temperature, salinity and the freezing rate as well as other factors [*Worster*, 1992b]. The mush Rayleigh number, Ra , is given by

$$Ra = \frac{g\Delta\rho\Pi h}{\kappa\eta}, \quad (1)$$

where g is the gravitational constant, $\Delta\rho$ is the brine density difference across the mush, Π is some representative permeability of the mush, h is a length scale such as the thickness of the mush, κ is the thermal diffusivity of the brine and η is the dynamic viscosity of the brine.

[7] Models that prognose sea-ice salinity and represent gravity drainage have been developed, but only recently are these beginning to appear in large-scale models. Based on measurements from *Cox and Weeks* [1975], *Cox and Weeks* [1988] were the first to design an empirical parameterization of gravity drainage. They introduced a drainage rate proportional to the vertical temperature gradient when the liquid fraction $\phi > 0.05$,

$$\frac{\Delta S_i}{\Delta t} = (A - B\phi) \frac{\Delta T}{\Delta z}, \quad (2)$$

where A and B are empirically fit parameters. They did not allow drainage to occur above impermeable layers. *Vancoppenolle et al.* [2007] used a modified version of this parameterization in their simulations of the landfast sea ice near Barrow, Alaska. A simpler gravity-drainage model was incorporated into the sea-ice model LIM [*Vancoppenolle et al.*, 2009a, 2009b]: the only state variable is vertically averaged bulk salinity per category; the vertical salinity profile is isohaline at high average bulk salinities and linear with zero at the upper surface for lower salinities. The gravity-drainage rate is a simple relaxation to 5 ppt with a timescale of 20 days. In 2010, *Vancoppenolle et al.* developed a gravity-drainage model featuring a diffusion operator, with a diffusivity that varies based on the critical mush Rayleigh number. Below $Ra_c = 10$, the diffusivity of salt is taken to be the molecular diffusivity; above 10, the diffusivity is 1000 times larger. A tanh function smooths the transition between those two states. When the ice is impermeable ($\phi < 0.05$), diffusion is zero.

[8] *Jeffery et al.* [2011] looked at gravity-drainage parameterizations for passive tracers rather than salinity. They modeled gravity drainage as an enhanced diffusion of salt using two alternative formulations for the effective salt diffusivity. The first increased the molecular diffusivity by an order of magnitude, while the second used mixing length theory to derive an enhanced salt diffusivity. The *Jeffery et al.* [2011] vertical transport model for tracers (including salt) is implemented in CICE using the original thermodynamics of *Bitz and Lipscomb* [1999].

[9] The present model incorporates an entirely new “mushy layer” thermodynamics formulation with fully implicit, tightly coupled temperature and salinity equations into CICE, as described in section 3. Mushy layer theory represents a liquid-solid mixture (“mush”) as a continuum by averaging separate equations for the liquid and solid constituents. The theoretical framework has been described in the sea ice context by *Feltham et al.* [2006] and *Hunke et al.* [2011], for example. We base a new parameterization of gravity drainage on behavior observed both in the field and in laboratory experiments [*Notz*, 2005; *Notz and Worster*, 2008], using mushy layer theory as a foundation. The laboratory and field measurements indicate that sea ice initially desalinates in two stages, beginning with an initial burst and then continuing to drain slowly. A similar gravity drainage parameterization has been developed simultaneously to the work presented here by *Griewank and Notz* [2011].

[10] The paper is organized as follows. In section 2, we describe the field and laboratory experiments. In section 3, we develop a dual mode parameterization of gravity drainage within a mushy layer formulation. Section 4 compares simulation results with the new thermodynamic model to the data, followed by a discussion of the model results in section 5.

2. Observations

[11] We use the laboratory and field measurements of *Notz* [2005] and *Notz and Worster* [2008] to guide our development of a gravity-drainage parameterization. These observations make use of an instrument capable of measuring the temporal evolution of bulk salinity at various depths within sea ice as it forms. The instrument consists of 14 pairs of platinum wires placed at various depths within the ice (6, 11, 18.5, 26, 36, 46, 56, 66, 81, 96, 111, 131, 151, and 171 mm below the upper ice surface). The electrical impedance is measured between the pairs and is used to infer the liquid fraction of the ice. The instrument also has a series of thermistors at the same depths as the wire pairs that record temperature, which is converted to brine salinity using a liquidus relation. With the measured liquid fraction and brine salinity, bulk salinity may be inferred. Although the instrument itself may influence the microstructure, estimates of bulk salinity as measured by the instrument agree well with theoretical estimates from mushy layer theory [*Notz*, 2005; *Notz et al.*, 2005].

[12] The first set of observations comes from a tank experiment [*Notz*, 2005] where salt water initially at a temperature of -1°C and salinity of 34 ppt is cooled from above at -10°C by a metal cooling plate. Bulk salinity, liquid fraction and temperature were recorded for 48 h after the experiment

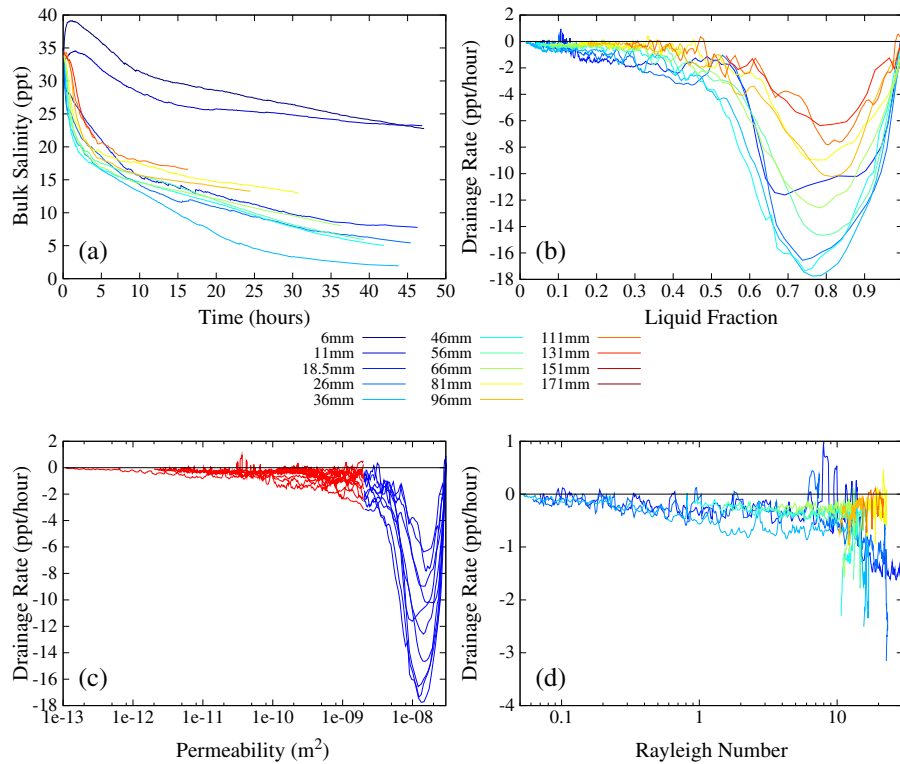


Figure 1. (a) Bulk salinity (ppt) versus time (hours) for the individual wire pairs in the tank experiment of Notz [2005]. The data for each depth is offset so that 0 h corresponds to when the ice/ocean interface reaches that depth. (b) Drainage rate (ppt/hour) versus liquid fraction for the tank experiment of Notz [2005]. Noise in the raw bulk salinity measurements makes calculating the time derivative difficult. In calculating drainage rates here and later, we first interpolate the data to a uniform time grid, then perform a running average over seven adjacent points. (c) Drainage rate (ppt/hour) versus permeability (m^2) for the experiment of Notz [2005]. The individual lines are divided by a permeability value of $5 \times 10^{-9} m^2$ into a rapid drainage mode (in blue) and a slow drainage mode (in red). (d) Drainage rate (ppt/hour) versus Rayleigh number for the experiment of Notz [2005]. Only the slow drainage mode (as shown by the red lines in Figure 1c) is shown in Figure 1d. Data from the top two sensors are removed in Figures 1a–1c.

began and ice started forming. The second set of experiments come from fieldwork in Adventfjorden in Spitsbergen during the winter of 2005 [Notz and Worster, 2008]. A 1×1 m hole was cut into existing sea ice and the instrument positioned in the water. The open water froze and bulk salinity was recorded. After ~ 140 h, the ice was removed from the hole and the measurements repeated for a further ~ 90 h as the open water refroze for a second time. In this way two periods of ice growth were recorded.

[13] Figure 1a shows bulk salinity versus time recorded during the tank experiment and fieldwork, respectively. The curves have been shifted in time so the origin of each curve is the time the growing ice/water interface first reached that particular depth as determined from the liquid fraction measurements at that depth. The legend underneath Figure 1a gives the color scheme used for all the plots in this paper showing results for the individual depths recorded by the instrument. The drainage clearly has two distinct modes. For all but the top two sensors, as ice first forms at a particular depth, the drainage rate is initially rapid and the bulk salinity drops from its initial value to ~ 20 ppt in a few hours. This process of rapid drainage near the ice base has been observed by Niedrauer and Martin [1979]. Drainage then proceeds at a much slower rate. The top two sensors

show unusual desalination behavior possibly caused by the very fast growth rate of the ice as it reached these sensors. This fast growth is likely to have led to structural inhomogeneities in the ice that caused difficulties for the derivation of bulk salinity from the raw data which depends on the precise determination of ice formation at a certain wire pair.

[14] These two distinct modes of drainage are also visible in Figure 1b where the drainage rate is plotted against liquid fraction. Again, the drainage rate is very high at early times when liquid fraction is high, but slows to a lower rate, with only a weak dependence on liquid fraction, until very low liquid fractions are reached. This behavior has been observed before [Weeks and Lee, 1958; Nakawo and Sinha, 1981]. Similar behavior is apparent for the fieldwork (Figure 2), which also exhibits two modes.

[15] Figures 1c and 2c show the drainage rate for the experiment and first period of fieldwork, respectively, versus the permeability of the sea ice, Π , as calculated by the formula of Freitag [1999]: $\Pi = 10^{-17} [10^3 \phi]^{3.1}$. The data has been divided by a permeability value of $5 \times 10^{-9} m^2$ for the experimental data and by $5 \times 10^{-10} m^2$ for the fieldwork data into two groups representing the rapid drainage mode (in blue) and the slow drainage mode (in red). These values of

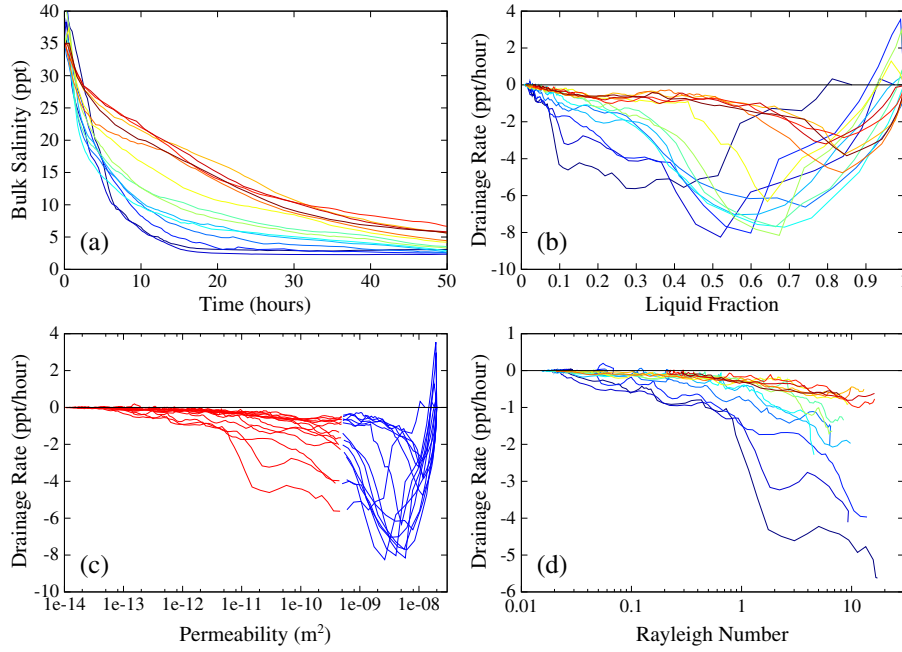


Figure 2. Same as Figures 1a–1d, but for the first field work period of *Notz and Worster* [2008]. In Figure 2c, the individual lines are divided by a permeability value of $5 \times 10^{-10} \text{ m}^2$ into a rapid drainage mode (in blue) and a slow drainage mode (in red).

permeability were chosen for illustration in these figures and are not used later.

[16] Figures 1d and 2d show drainage rate versus mush Rayleigh number for the slow drainage mode, as shown by the red lines in Figures 1c and 2c. The mush Rayleigh number is calculated from equation (1) using the permeability equation of *Freitag* [1999] for Π . Slow drainage appears to occur even though the Rayleigh number is below the canonical critical value of around 10. In fact, for this drainage, there is no apparent cutoff in drainage rate at a particular Rayleigh number. However, the upper limit of this mode of drainage does occur at a Rayleigh number of order 10, suggesting that this value does regulate the rapid drainage mode.

3. Mushy Layer Formulation

[17] The structure of sea ice consists of microscopic brine inclusions surrounded by a fresh ice crystal matrix. A popular method for describing this type of structure is called mushy layer theory [e.g., *Worster*, 1992a; *Feltham et al.*, 2006; *Hunke et al.*, 2011]. In mushy layer theory, separate equations for the brine and ice matrix are averaged over a region to make a continuum model. The region is large enough to capture a representative sample of brine pockets and ice matrix, yet small enough that the region has a single porosity.

[18] Conservation equations can be formulated and solved for the mush enthalpy and bulk salinity. The ice temperature is then determined from the enthalpy and bulk salinity. The vertical heat conservation equation is given by

$$\frac{\partial q}{\partial t} + v_z \frac{\partial q_{\text{br}}}{\partial z} = \frac{\partial}{\partial z} \left(K \frac{\partial T}{\partial z} \right) + F_{\text{swabs}}, \quad (3)$$

where the second term on the left hand side represents the vertical advection of heat by the flow of brine through the mush, the first term on the right hand side represents conduction of heat, and the second term on the right hand side represents the absorbed shortwave radiation. q is the enthalpy of the mush (the negative of the energy required to raise the temperature of the mush to 0°C and melt any ice), t is time, T is the temperature of the mush in $^\circ\text{C}$, K is the thermal conductivity of the mush, v_z is the upwards vertical Darcy velocity for flow through the mush, q_{br} is the brine enthalpy, and z is the vertical position in the ice, zero being at the lower ice surface and increasing upward. Simultaneously with the heat conservation equation, we solve a salt conservation equation:

$$\frac{\partial S}{\partial t} + v_z \frac{\partial S_{\text{br}}}{\partial z} = \frac{\partial S}{\partial t} \Big|_{\text{slow}} \quad (4)$$

where S is the bulk salinity and S_{br} is the brine salinity. The second term on the left represents the advection of salt by a vertical flow of brine through the mush, while the term on the right represents sources or sinks of bulk salinity.

[19] Properties for the mush are then determined from a volume average of individual properties for the ice and for the brine. If χ_i is the value of a property for the ice in some region and χ_{br} is the value of that property for the brine in that region, then the value of the property for the mush, χ , in the region is

$$\chi = \phi \chi_{\text{br}} + (1 - \phi) \chi_i \quad (5)$$

where ϕ is the volume fraction of brine in the mush. Thus, the average salinity of the ice and brine in the mush, termed bulk salinity, S , is related to the salinities of the ice, S_i , and brine, S_{br} , by

$$S = \phi S_{\text{br}} + (1 - \phi) S_i. \quad (6)$$

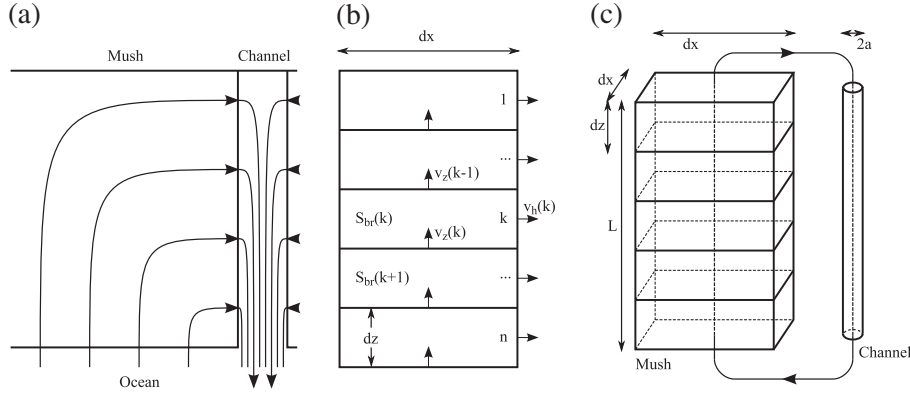


Figure 3. Schematics of the gravity-drainage parameterization. (a) Conceptualized flow in the mush with up-flow in the mush and down-flow in a channel. (b) Parameterization grid with horizontal averaging and channel neglected. $v_z(k)$ represents the vertical flow into layer k , and $v_h(k)$ the horizontal component into the channel. The number of layers is fixed. (c) Flow explicitly calculated in mush and channel.

The ice matrix, however, is almost fresh and we take $S_i = 0$, which means

$$\phi = \frac{S}{S_{br}}. \quad (7)$$

Neglecting gas inclusions, ϕ is a measure of the sea-ice porosity.

[20] We assume that the density of ice and brine is the same except where the density difference generates a buoyancy force during gravity drainage. This is why no densities appear in equation (6). Therefore, we neglect brine expulsion due to expansion of ice during freezing, an assumption justified by *Notz and Worster* [2009], who found that expulsion does not contribute significantly to desalination.

[21] The small size of the brine inclusions allows them to adapt very rapidly to changes in temperature and brine salinity. A brine inclusion of size δ will adapt in a time $t \sim \delta^2/D_b$ where D_b is the diffusivity of salt in the brine. Typical values for sea ice are $\delta \sim 10^{-4} - 10^{-3}$ m and $D_b \sim 10^{-9}$ m²s⁻¹ so that thermodynamic equilibrium is achieved after 10 s to 10³ s, a timescale much smaller than the timescale of diurnal variation found in sea ice [*Feltham et al.*, 2006]. The ice and brine are assumed to be in thermodynamic equilibrium, resulting in the temperature always being at the liquidus temperature of the brine,

$$T = T_L(S_{br}). \quad (8)$$

This thermodynamic equilibrium is achieved physically by an appropriate amount of phase change occurring between ice and liquid water as the temperature or brine salinity change. It is common practice to use a linear liquidus relation for sea water, such as $T_L = -0.054S_{br}$ currently used in CICE. This gives good results at near-freezing temperatures but overestimates the equilibrium brine salinity at lower temperatures by >50% at -20°C . Instead, we use the piecewise linear relation of *Assur* [1958], which reduces errors to <20% at these lower temperatures (see Appendix A for details).

[22] For calculating the vertical thermodynamics, we separate the calculation of temperature and salinity evolution from that of the thickness. First, the temperature and salinity are evolved while the thickness is kept fixed. Then, using the updated temperatures and salinities, growth and melting of the upper ice surface and base are calculated. We discretize

the heat and salt conservation equations using a finite volume formulation that conserves energy and salt content. We use an upwind scheme to discretize advection operators. The discretized layer thickness is fixed while solving the heat and salt conservation equations and is constant throughout the ice column. The calculation of growth and melting leaves the layers with uneven thicknesses, which are adjusted after this calculation in a conserving manner to return them to even thicknesses. The enthalpy and salinity equations form a set of nonlinear coupled equations, solved implicitly using a Jacobian Free Newton Krylov (JFNK) method [*Knoll and Keyes*, 2004]. We precondition the JFNK solver with the Jacobian of the system calculated with salinity variations set to zero and the thermal conductivity constant at the previous time step value.

3.1. Rapid Drainage Mode

[23] Since this mode of drainage appears to occur when the Rayleigh number is above a critical value, we base our parameterization on a mush Rayleigh number formulation. Convection in mushy layers is believed to proceed by an upward flow of brine through the mush and a downward flow of brine through channels empty of ice crystals (termed chimneys in the mushy layer literature), which are much larger than the macroscopic brine inclusions in the mush (see Figure 3a). When convection in the mush first develops, the downward flow of brine is through mush, but being advected from higher in the ice, this brine is salty and tends to dissolve the ice crystal matrix to form channels [*Worster*, 1991].

[24] In our parameterization, the mush and channel are each horizontally averaged, leaving a purely upward flow in the mush, a purely downward flow in the channel and a purely horizontal flow connecting the mush to the channel. The horizontal size of the channel is much smaller than that of the mush (and has correspondingly higher brine velocities) and thus accounts for a much smaller fraction of the bulk sea-ice volume than the mush. In calculating changes in the bulk salinity of sea ice, we therefore neglect the contribution of salt in the channels since their relative volume is so low (see Figure 3b), and brine entering the channel from the mush is assumed to instantaneously flow to the ocean. Under these assumptions, the channels are not included in

the mush, which is governed by the thermal equilibrium assumption of mushy layer theory.

[25] With these assumptions, the change in the bulk salinity of the sea ice, due to gravity drainage, is caused by the upward advection of brine in the sea ice, so that

$$\frac{\partial S}{\partial t} = -v_z \frac{\partial S_{br}}{\partial z}. \quad (9)$$

The velocity, v_z , in the mush is a Darcy velocity, which is an average of the vertical velocity in the brine inclusions over the local porous structure. The upward flow of brine also causes a transport of brine enthalpy, so an equivalent equation to equation (9) is applied as an advective term in the heat equation (3), i.e.,

$$\left. \frac{\partial q}{\partial t} \right|_{\text{advection}} = -v_z \frac{\partial q_{br}}{\partial z}. \quad (10)$$

Here q is the enthalpy of the mush while q_{br} is the enthalpy of the brine. The parameterization is completed by specifying v_z . P. Griewank and D. Notz have developed a similar parameterization for gravity drainage based on a mush Rayleigh number whose flow strength is derived from the work of Wells *et al.* [2010] (personal communication).

[26] We base our derivation of v_z on a “local” Rayleigh number. As originally derived, the Rayleigh number provides an indication of whether the form of heat transfer within the mush is conductive or convective. A local Rayleigh number can also be used which describes the tendency of a layer within the mush to undergo convection [Notz and Worster, 2008]. The local Rayleigh number is defined as in equation (1), but $\Delta\rho$ is the density difference between the layer in question and the ocean, Π is the minimum mush permeability at or beneath the layer and rather than using the total mush thickness, h , for the length scale, the distance from the individual layer to the ocean, l , is used. The local mush Rayleigh number goes to zero as the interface is approached, since Ra is proportional to l . This does not mean that subcritical layers between the layer and the ocean prevent a layer above from convecting (there will always be such subcritical layers). Convection is a non-local phenomenon and flow can occur at a place with a subcritical density difference if it is driven by a super-critical density difference elsewhere in the ice. Consequently, a layer with a super-critical Rayleigh number will drive a convective flow in all layers between it and the ocean.

[27] To accommodate this non-local nature of the convection, for each layer, we calculate an individual vertical flow, \tilde{v} , from the ice base to that layer based on the local Rayleigh number of that layer. For the layer in question \tilde{v} represents a flow rate, driven by conditions at that layer, that occurs in all layers between that layer and the ocean. A layer near the bottom of the ice will have multiple flow velocities due to conditions in layers higher in the ice. This represents the non-local nature of convection, described in the preceding paragraph, where layers high in the ice can drive a convective flow in layers below them. Once these individual flow rates are calculated, they must be combined to form the total flow rate, v_z . We choose the flow rate of a layer to be the largest of the flow rates calculated for layers above it and its own flow rate:

$$v_z(k) = \max_{j=k,n} (\tilde{v}(j)) \quad (11)$$

where $j = 1$ is the lowest layer and $j = n$ is the uppermost layer. In the next two sections, we introduce two separate fast-mode brine drainage parameterizations that calculate the individual flow rates \tilde{v} for the ice layers. The first one, without considering channels, produces unrealistically large v_z , thus leading us to the second parameterization, with channels. In what follows, l is the distance from the ocean to the top of the layer for which \tilde{v} is being calculated for.

[28] A Rayleigh number formulation for the mush without channels. The Rayleigh number can be thought of as a ratio of the timescale for the convection of heat, τ_{conv} , and the timescale for the conduction of heat, τ_{cond} :

$$Ra = \frac{\tau_{\text{cond}}}{\tau_{\text{conv}}}. \quad (12)$$

For a timescale of conduction much smaller than that of convection (small Rayleigh number), conduction will dominate and convection will not occur. For a timescale of conduction greater than that of convection (large Rayleigh number), convection will dominate conduction. The timescale of conduction for a given length scale l is given by $\tau_{\text{cond}} = l^2/\kappa$, whereas that for convection to given by $\tau_{\text{conv}} = l/v_{\text{conv}}$ where v_{conv} is some characteristic flow speed of convection in the absence of conduction (\tilde{v} is the convective speed when conduction is present). Applying these timescales in equation (12), we have

$$v_{\text{conv}} = \frac{\kappa Ra}{l}. \quad (13)$$

[29] We can use equation (13) to derive an approximate formula for the actual velocity when conduction is also present, \tilde{v} . At a critical Rayleigh number Ra_c , the actual velocity becomes zero, while at very high Rayleigh numbers, we expect conduction to be unimportant and the actual velocity \tilde{v} , to be close to v_{conv} . A simple relation with these limits is

$$\tilde{v}(z) \simeq v_{\text{conv}} \left(\frac{Ra(z) - Ra_c}{Ra(z)} \right), \quad (14)$$

or using equation (13)

$$\tilde{v}(z) \simeq \kappa \left(\frac{Ra(z) - Ra_c}{l} \right), \quad (15)$$

where l is the distance to the layer at z from the ocean. Wells *et al.* [2010] found a linear relationship between flux and Rayleigh number, while for a non-reactive porous media, Nield and Bejan [2006] show convective flux proportional to $Ra^{0.5}$.

[30] This equation has no free parameters but tends to produce a very rapid drainage velocity, because the flow in the channel is neglected. To see this, consider the energy dissipation per unit volume in the mush from viscous forces, given by $\epsilon_0 = (\eta \tilde{v}^2)/\Pi$ [Phillips, 1991], and the energy dissipation per unit length of a circular-cross-section channel of radius a with Poiseuille flow, $\Phi = 8\eta Q^2/\pi a^4$, where Q is the flow rate in the channel [Batchelor, 1967]. By conservation of volume, the flow rising in the mush must be balanced by the downward flow in the channel such that $\tilde{v} \Delta x^2 = Q$, where the mush has been assumed to be a square column of base width Δx . The energy dissipated per unit height of mush is then

$$E_{\text{mush}} = \frac{\eta \tilde{v}^2 \Delta x^2}{\Pi}, \quad (16)$$

while energy dissipation per unit height of channel is

$$E_{\text{channel}} = \frac{8\eta\tilde{v}^2\Delta x^4}{\pi a^4}. \quad (17)$$

The ratio of dissipation per unit depth in the channel versus the mush is, therefore,

$$R = \frac{E_{\text{channel}}}{E_{\text{mush}}} = \frac{8\Delta x^2\Pi}{\pi a^4}. \quad (18)$$

Taking $\Pi \sim 3 \times 10^{-8} \text{ m}^2$, $a \sim 0.5 \text{ mm}$ and $\Delta x \sim 1 \text{ cm}$, the ratio becomes $R \sim 120$. Thus, dissipation of energy in the channel is much larger than in the mush and cannot be neglected. Without it, the total dissipation is under-predicted when compared to the release of gravitational energy, and the velocity over-predicted.

[31] *A new formulation including the channels.* We now present a more rigorous method for determining the vertical velocity in the mush, in which the flow is considered in the down-flowing channel as well as in the mush. Figure 3c shows the model setup. Brine is assumed to flow upward through a thickness l of mush and then down a channel of diameter $2a$ with no horizontal connection between them except at the ends. This represents the flow generated by a single layer in the ice, with the top of that layer being a distance l above the ice/ocean interface. The calculation is repeated for all layers and integrated to form the final flow used for the upwards advection in the mush.

[32] We assume that the resistance to the flow occurs in the vertical direction in the mush and the channel, and, therefore, the pressure difference between the top of the layer and the bottom of the mush must be the same as that in the channel. We assume, because the channel is so much larger than the brine inclusions in the mush and the salt diffusivity so low, that brine entering the channel remains unmodified in salinity as it travels out of the ice to the ocean. Hence, the salinity of brine in the channel associated with layer l is constant and equal to the value at the top of the height l of mush (this corresponds to the average of the salinities of the top layer in the height l of mush and the layer above). Thus, the average density in the channel is higher than that in the mush, and it is this density difference that drives a circulating flow. In particular, the difference in hydrostatic pressure through the mush is $\Delta P_h^m = -g \int_0^l \rho_m dz$. In the channel, it is $\Delta P_h^p = -g \int_0^l \rho_p dz = -g\rho_p l$, so $|\Delta P_h^p| > |\Delta P_h^m|$. The actual pressure difference (which is the same across the length of the channel and the mush) lies between ΔP_h^m and ΔP_h^p . Thus, in the mush, the magnitude of the actual pressure difference is greater than the magnitude of the hydrostatic pressure difference leading to an upward flow in the mush, whereas in the channel, the magnitude of the pressure difference is less than the magnitude of the hydrostatic pressure difference in the channel leading to a downward flow there. The channels initially form by dissolution of the ice matrix by the downward moving brine (not by melting because the downward flow is cold but salty). As an approximation, we assume that to first order after the channels are formed, the brine flows within them rapidly enough that its salinity is not altered via non-equilibrium effects. In reality, the brine channels will to some extent refreeze and remelt after their formation as was observed by *Niedrauer and Martin* [1979].

[33] We first derive the vertical flow, excluding the effect of thermal conduction v in the mush to height l driven by a pressure difference ΔP across l . We then modify this flow to obtain \tilde{v} , the flow with the effect of thermal conduction considered. The mush is assumed to have n layers, each with different permeabilities $\Pi(k)$, and brine densities $\rho(k)$. Conservation of flow means v is the same in each layer so, from Darcy's equation, in each layer

$$v = \frac{\Pi(k)}{\eta} \left(-\frac{\Delta P(k)}{\Delta z} - \rho(k)g \right), \quad (19)$$

where $\Delta P(k)$ is the pressure difference across the layer, which has thickness Δz . Rearranging,

$$\Delta P(k) = -\frac{v\eta\Delta z}{\Pi(k)} - \rho(k)g\Delta z. \quad (20)$$

We can add the individual layer pressure differences to get an expression for the pressure difference across the mush thickness l :

$$\Delta P = \sum_{k=1}^n \Delta P(k), \quad (21)$$

$$\Delta P = -v\eta\Delta z \sum_{k=1}^n \frac{1}{\Pi(k)} - g\Delta z \sum_{k=1}^n \rho(k). \quad (22)$$

Thus, in terms of the pressure difference across the mush, the velocity, v , is given by

$$v = \frac{n}{\eta \sum_{k=1}^n \frac{1}{\Pi(k)}} \left(-\frac{\Delta P}{l} - \frac{g}{n} \sum_{k=1}^n \rho(k) \right), \quad (23)$$

where $l = n\Delta z$.

[34] Defining two variables, A_m and B_m , this can be more compactly written as

$$v\Delta x^2 = A_m \left(-\frac{\Delta P}{l} + B_m \right), \quad (24)$$

where

$$A_m = \frac{\Delta x^2}{\eta} \frac{n}{\sum_{k=1}^n \frac{1}{\Pi(k)}}, \quad (25)$$

$$B_m = -\frac{g}{n} \sum_{k=1}^n \rho(k). \quad (26)$$

[35] The channel has a circular cross section with radius a . We assume the flow in the channel is laminar, dominated by viscous forces, and is described by Poiseuille flow. The flow rate in the channel is given by [*Batchelor*, 1967]

$$Q = \frac{\pi a^4}{8\eta} \left(-\frac{\Delta P}{l} - \rho_p g \right), \quad (27)$$

where ρ_p is the density of brine in the channel and ΔP is, as assumed earlier, the same pressure difference as that across the mush. This can also be more compactly written as

$$Q = A_p \left(-\frac{\Delta P}{l} + B_p \right), \quad (28)$$

with

$$A_p = \frac{\pi a^4}{8\eta}, \quad (29)$$

$$B_p = -\rho_p g. \quad (30)$$

[36] Brine rises in the mush with Darcy velocity v and then sinks in the channel with flow rate Q . We assume

the mush has a square horizontal cross section with side $\Delta x \gg a$. By conservation of flow $v\Delta x^2 = -Q$. Equating equations (24) and (28), we have

$$\frac{\Delta P}{l} = \frac{A_p B_p + A_m B_m}{A_m + A_p}. \quad (31)$$

The mush velocity can be calculated with equation (24), or equivalently with equation (28).

[37] This velocity must then be moderated by the Rayleigh number so that flow only occurs when the Rayleigh number is above some critical value. We choose

$$\tilde{v}(z) = v \left(\frac{Ra(z) - Ra_c}{Ra(z)} \right), \quad (32)$$

where Ra_c is the critical Rayleigh number.

[38] This rapid drainage mode parameterization has three tunable parameters, all with physical meaning. We take the diameter of the channel to be 1 mm, so $a = 0.5$ mm. We assume that Δx is proportional to the thickness l of the column so that $\Delta x = 2\beta l$. We take $\beta = 1$, a value that gives a square aspect ratio for the convective flow in the mush, which is an aspect ratio often approximately found in convective flows [Worster, 1992b]. We take Ra_c to be 10, an approximate value suggested by Notz and Worster [2008]. In reality, not all of these parameters are independent; for example, the actual size of convection cells will depend on Ra_c . A deeper treatment would not be tractable in global climate models at the present time and is beyond the scope of this study.

3.2. Slow Drainage Mode

[39] The slow drainage mode is more difficult to interpret physically. The drainage rate is not a strong function of permeability (Figures 1c and 2c) and drainage occurs at low values of the Rayleigh number (Figures 1d and 2d). This suggests that the flow is not associated with mush Rayleigh convection. One possibility is that both upwards and downwards flow of brine occurs in channels during this mode of drainage. In this scenario, draining brine would flow from the interior of the mush to nearby pre-existing channels, possibly partly driven by brine expulsion. Niedrauer and Martin [1979] observed strong convection in a thin layer at the ice/ocean interface, while bidirectional flow of brine in channels drained the deeper ice interior. The slanting drainage channels were observed to migrate horizontally through the ice due to temperature and salinity gradients within the bidirectional flow, potentially draining a larger area of ice interior than would static channels. Both an upward and downward flow of brine was also observed in brine channels by Eide and Martin [1975], and the flow was oscillatory. Within our model, the rapid desalination mode represents the convection seen near the ice/ocean interface by Niedrauer and Martin [1979] while the bi-directional brine flow is represented by the slow drainage mode. In the absence of a theoretical understanding of this slow drainage process, we choose to parameterize it via a source term in the salinity conservation equation.

[40] For salinities less than 20 ppt, the bulk salinity versus time profiles can be reasonably well fitted with exponential decay curves. We choose to parameterize this slow drainage

with a simple relaxation of the bulk salinity to some low limiting value, similarly to Vancoppenolle et al. [2009a]:

$$\left. \frac{\partial S(z)}{\partial t} \right|_{\text{slow}} = -\lambda(S(z) - S_c). \quad (33)$$

We model the decay constant, λ , as

$$\lambda = \omega \max \left(\frac{T_{\text{bot}} - T_{\text{sfc}}}{h}, 0 \right), \quad (34)$$

where ω is a tuning parameter for strength of drainage, T_{bot} is the bottom interface temperature, T_{sfc} is the upper surface temperature and h is the ice thickness. This formulation only allows drainage if there is an unstable temperature gradient across the ice. The bulk salinity relaxes to a value of $S_c(z)$ given by

$$S_c(z) = \phi_c S_{\text{br}}(z), \quad (35)$$

where ϕ_c is a critical porosity at which the ice becomes permeable. We use a value of 0.025 here to fit the low final salinities found in the observations. In other simulations, a more canonical value of 0.5 [Golden et al., 2007] might be more appropriate.

[41] Conceptually, we can think of this process as sea water rising up a channel to a given layer and replacing brine in the mush, which flows out to the ocean down the same channel. We assume that, because of the low diffusivity of salt, brine can flow with unmodified salinity in the relatively wide channels. The vertical flow strength of brine in the channels averaged horizontally over all the ice $|v|$, corresponding to the above drainage parameterization is given by

$$\left. \frac{\partial S(z)}{\partial t} \right|_{\text{slow}} = |v| \frac{(S_{\text{oce}} - S_{\text{br}}(z))}{\Delta z}. \quad (36)$$

There is both an upward flow and downward flow of strength $|v|$. This flow occurs from the layer in question to the ocean and passes through all the intermediate layers in the ice. Similar flows are generated by each layer undergoing drainage and must be integrated to obtain the total flow. $|v|$ can be calculated from equation (36) using the drainage rate from equation (33).

[42] In addition to moving salt, these flows transport heat around the sea ice and must be taken into account in the heat conservation equation (3). While the low salt diffusivity allows brine in the channel to travel without changes in its salinity, the thermal diffusivity in the brine is much larger. Therefore, we assume that the temperature of the brine adapts rapidly to the local temperature of the mush as it moves vertically. The brine in the channels will therefore have the brine enthalpy, q_{br} , of the local temperature. Layers in the ice beneath the layer in question will experience a flow of brine from above, v_{\uparrow} , and an identical flow of brine from below, v_{\downarrow} , where $|v| = |v_{\downarrow}| = |v_{\uparrow}|$. $|v|$ is given by equation (36). Then the change in incremental time Δt of the energy content of that layer will be

$$\begin{aligned} \Delta E = \Delta z \Delta q = & |v_{\uparrow}| \Delta t (q_{\text{br}}(k-1) - q_{\text{br}}(k)) \\ & + |v_{\downarrow}| \Delta t (q_{\text{br}}(k+1) - q_{\text{br}}(k)), \end{aligned} \quad (37)$$

where the first term on the right hand side corresponds to the effect of flow from the layer beneath and the second term on

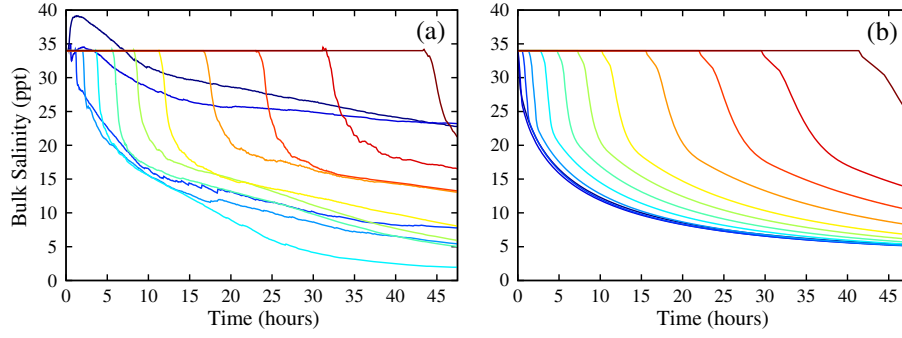


Figure 4. Bulk salinity (ppt) versus time (hours) for (a) the individual wire pairs in the tank experiment of Notz [2005], and (b) the corresponding model simulation with 100 layers. Model data is interpolated to the same depths as the wire pairs in the experiment.

the right hand side corresponds to the effect of flow from the layer above. Thus, the change in enthalpy of that layer is

$$\frac{\Delta q}{\Delta t} = |\nu| \Delta z \frac{(q_{br}(k+1) - 2q_{br}(k) + q_{br}(k-1)))}{\Delta z^2}, \quad (38)$$

which is just a discretized version of the heat diffusion equation

$$\frac{\partial q}{\partial t} = K \frac{\partial^2 T}{\partial z^2} \quad (39)$$

with the conductivity given by

$$K = \Delta z^2 \rho_{br} c_{br} \left. \frac{\partial S}{\partial t} \right|_{slow} \frac{1}{S_{ocn} - S_{br}}. \quad (40)$$

Thus, the thermal effect of the slow drainage is an extra heat diffusion term. The effect of the drainage of all the layers can be integrated and added to the heat equation (3). The effect is found to be much smaller than regular thermal conductivity ($< 1\%$).

4. Simulation Results

[43] We use the numerical scheme described in section 3 with the two gravity-drainage parameterizations described in sections 3.1 and 3.2 to simulate the experiment of Notz [2005] and the fieldwork of Notz and Worster [2008]. We solve conservation equations for enthalpy and bulk salinity simultaneously using an implicit Newton method. We assume both gravity-drainage processes are available all

the time, often acting simultaneously, but when the rapid drainage ends, the slow drainage continues.

4.1. Laboratory Experiment

[44] We simulate the gravity-drainage tank experiment of Notz [2005], performing experiments with 100, 10 and four vertical layers and an initial ice thickness of 1 cm. One hundred layers resolve the vertical gradients well, while 10 layers is more likely to be feasible in climate simulations. Currently, CICE uses four layers. For simulations with 100 layers, we use a timestep of 90 s, while for simulations with 10 or four layers, we use a timestep of 900 sec. The initial bulk salinity of the ice is set to 34 ppt, the initial tank salinity during the experiment. The initial temperature profile in the ice is linear in the model with the upper surface temperature fixed at -10°C for the duration of the experiment and the base temperature at the freezing temperature of the initial tank salinity using equation (A5). Since we lack a model of the heat flow in the water near the ice in this test, we set the heat flow from water to the ice to zero and fix the ice/ocean interface solid fraction ($1 - \phi_i$ in equation (A9)) to 0.15. This value reproduces the observed ice thickness growth rate.

[45] Figure 4 shows the bulk salinity at various depths versus time as measured by the wire pair instrument in Notz [2005]. Also plotted are the 100 layer model results, which have been interpolated to the constant depths of the instrument wire pairs to allow a comparison. The model does a good job of reproducing the experimental results.

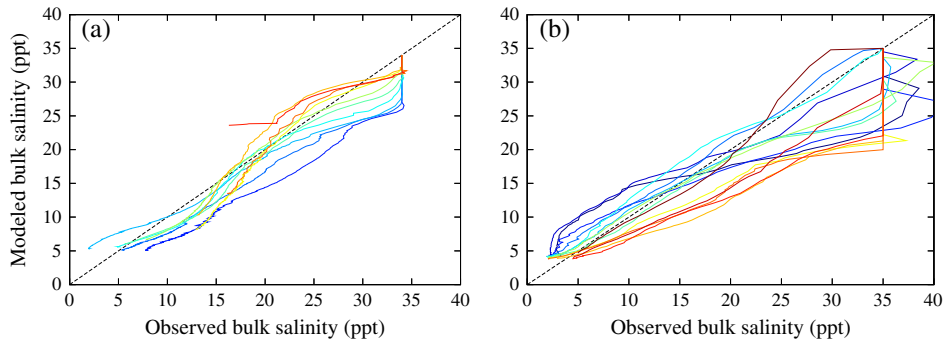


Figure 5. Modeled bulk salinities (ppt) versus observed bulk salinities (ppt) for (a) the experiment of Notz [2005] and (b) the fieldwork of Notz and Worster [2008].

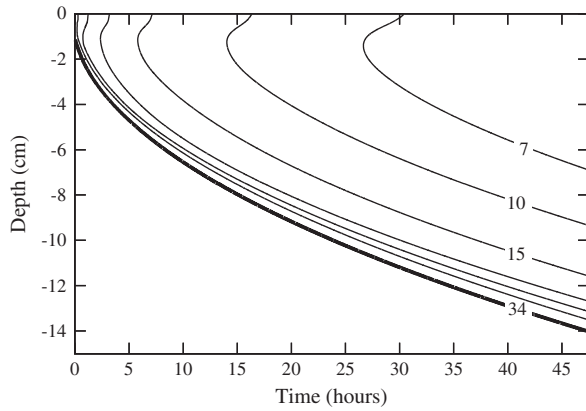


Figure 6. Contour plot of bulk salinity (ppt) versus time (hours) and depth (cm) for the model simulation of the experiment of *Notz* [2005] with 100 layers. The bold line signifies 34 ppt, which represents the ice base. Lines with missing labels are at 20, 25 and 30 ppt with salinity values increasing downwards.

Two modes of drainage are clearly visible in the model results and the general shape of the curves is similar. As described in section 2, the two instrument depths nearest the upper surface in the data exhibit curious behavior that is not fully understood and not present in the model. Figure 5a shows a plot of modeled bulk salinity versus observed bulk salinity. The reasonable fit of the model to the experimental data is evident in this figure.

[46] Figure 6 presents a different view of the model results. Evident in this plot is that the rapid drainage mode occurs in a thin region just above the ice/ocean interface while the slow drainage occurs throughout the ice. The model also reproduces a weak “C” shaped profile at early times with increased salinity near the surface. The problems with the top two sensors prevent an evaluation of this aspect of the model. Bulk salinity profiles at 4, 12,

24, 36, and 48 h for both the experiment and the model are presented in Figure 7, with reasonable agreement between model and experiment. Figure 7a shows the experimental results. Figure 7b shows the model results using 100 layers in the vertical, interpolated to the same depths as the experiment instrument. Figures 7c and 7d show the model output with 10 layers and four layers, respectively, more typical of that used in global climate models. Because of the low resolution, the models with 10 layers and four layers do not have a thin enough early drainage region next to the ice/ocean interface, as expected.

4.2. Fieldwork

[47] We simulate the fieldwork of *Notz and Worster* [2008] performing experiments with 100, 10 and four layers in the vertical and an initial ice thickness of 1 cm. As in section 4.1, for simulations with 100 layers, we use a timestep of 90 sec, while for simulations with 10 or four layers, we use a timestep of 900 sec. We assume the ice is initially composed of frazil ice, which would be expected for ice formation in open water in the Arctic and requires process parameterizations beyond the scope of this study. We assume this frazil layer is well mixed (isothermal) and has a constant initial liquid fraction. *Smedsrud and Skogseth* [2006] and *Naumann et al.* [2012] found initial liquid fractions of around 0.75 for newly formed grease ice. *Naumann et al.* [2012] also found initial bulk salinities about 3 ppt less than the ocean salinity. We use these values for our initial liquid fraction and bulk salinity. This implies that the brine salinity is higher than the ocean salinity, contrary to what was assumed by *Smedsrud and Skogseth* [2006] where they were assumed equal. *Naumann et al.* [2012], however, using different methods found some evidence for a difference of 7 ppt, while *Maus and De La Rosa* [2012] found little observational evidence for a difference greater than 2 ppt in grease ice. Clearly, further work is required on this frazil ice initial condition. The initial temperature is taken as the freezing temperature of the interstitial brine.

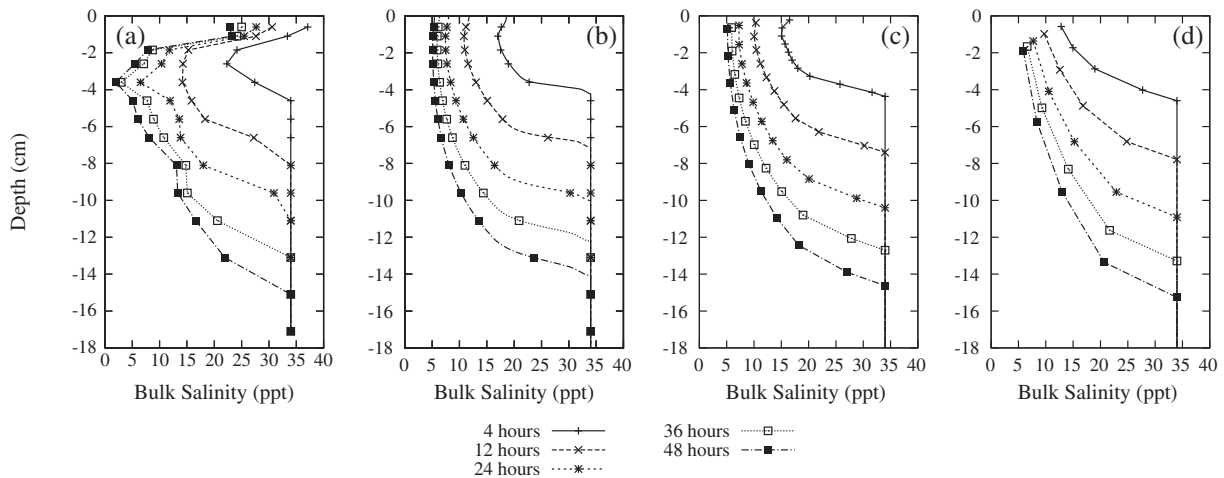


Figure 7. Vertical profiles of bulk salinity (ppt) at 4, 12, 24, 36, and 48 h. (a) Experimental data of [Notz, 2005]. (b) Corresponding model simulation results (section 4.1) with 100 layers in the vertical. The points show the model data interpolated to the same depths as the wire pairs in the experiment. (c) Model simulation results with 10 layers in the vertical. No interpolation is performed and grid cell values are presented. The lowest point in each profile represents the ice/ocean interface position. (d) Same as in Figure 7c but with four layers in the vertical.

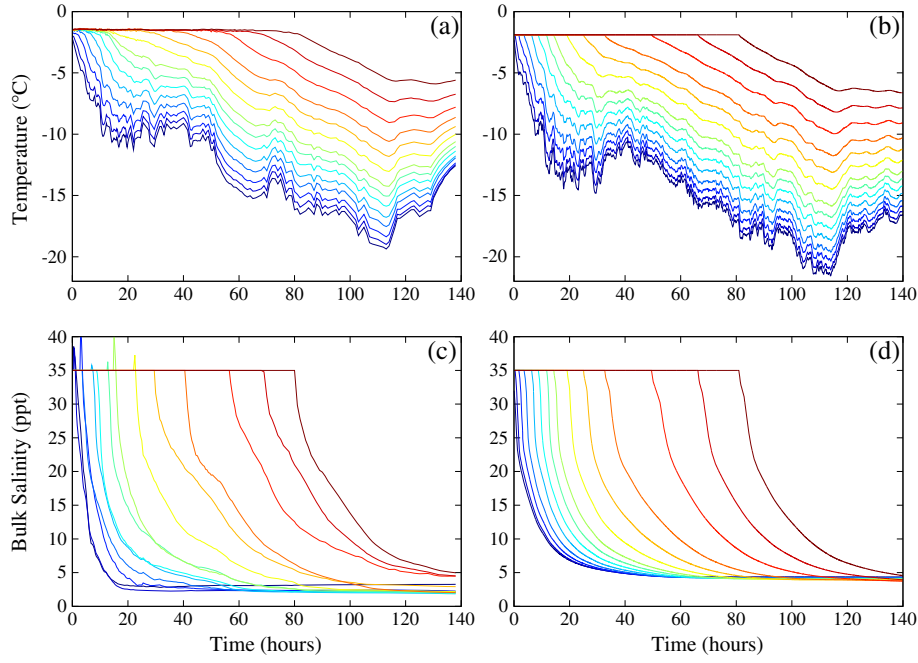


Figure 8. Temperature (°C) versus time (hours) for (a) the individual wire pairs in the fieldwork of Notz and Worster [2008], and (b) the corresponding model simulation with 100 layers. Bulk salinity (ppt) versus time (hours) for (c) the individual wire pairs in the fieldwork of Notz and Worster [2008], and (d) the corresponding model simulation with 100 layers. Model data is interpolated to the same depths as the wire pairs in the experiment.

[48] We set the ocean salinity to 35 ppt. No measurements of ocean salinity were recorded, but a value of approximately 35 ppt is obtained from the maximum bulk salinities measured by the wire pair instrument, which cannot directly measure ocean salinity. The ocean temperature we take as the temporal average of the temperature recorded by the deepest wire pair on the instrument during the first 40 h of each fieldwork period. This wire pair was below the

ice/ocean interface during that period. The transfer of heat to the ice/ocean interface from the ocean is calculated from the difference in ocean and ice bottom temperature using the bulk transfer formula used by CICE:

$$F_{\text{bot}} = -c_h c_{\text{ocn}} \rho_{\text{ocn}} u_* (T_{\text{ocn}} - T_{\text{bot}}), \quad (41)$$

where F_{bot} is the heat transfer from the ocean, $c_h = 0.006$ is a heat transfer coefficient, c_{ocn} is the ocean heat capacity,

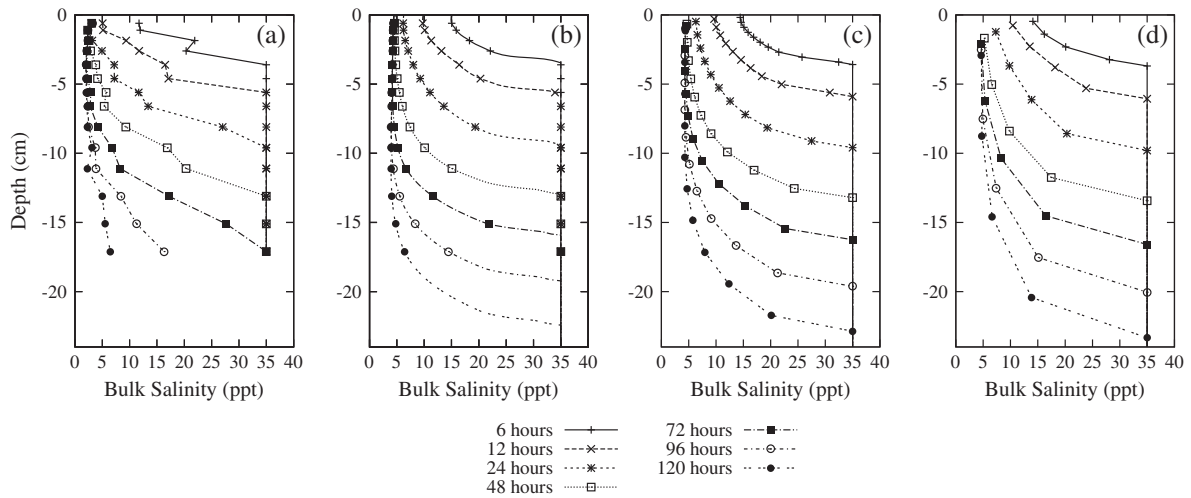


Figure 9. Vertical profiles of bulk salinity (ppt) at 6, 12, 24, 48, 72, 96 and 120 h. (a) Fieldwork data of Notz and Worster [2008]. (b) Model simulation results of section 4.2 with 100 layers in the vertical. The points show the model data interpolated to the same depths as the wire pairs in the experiment. No measurements are displayed deeper than 17 cm in Figures 9a and 9b since this was the maximum depth of the instrument. (c) Model simulation results (section 4.2) with 10 layers in the vertical. No interpolation is performed and grid cell values are presented. (d) Same as in Figure 9c but with four layers in the vertical.

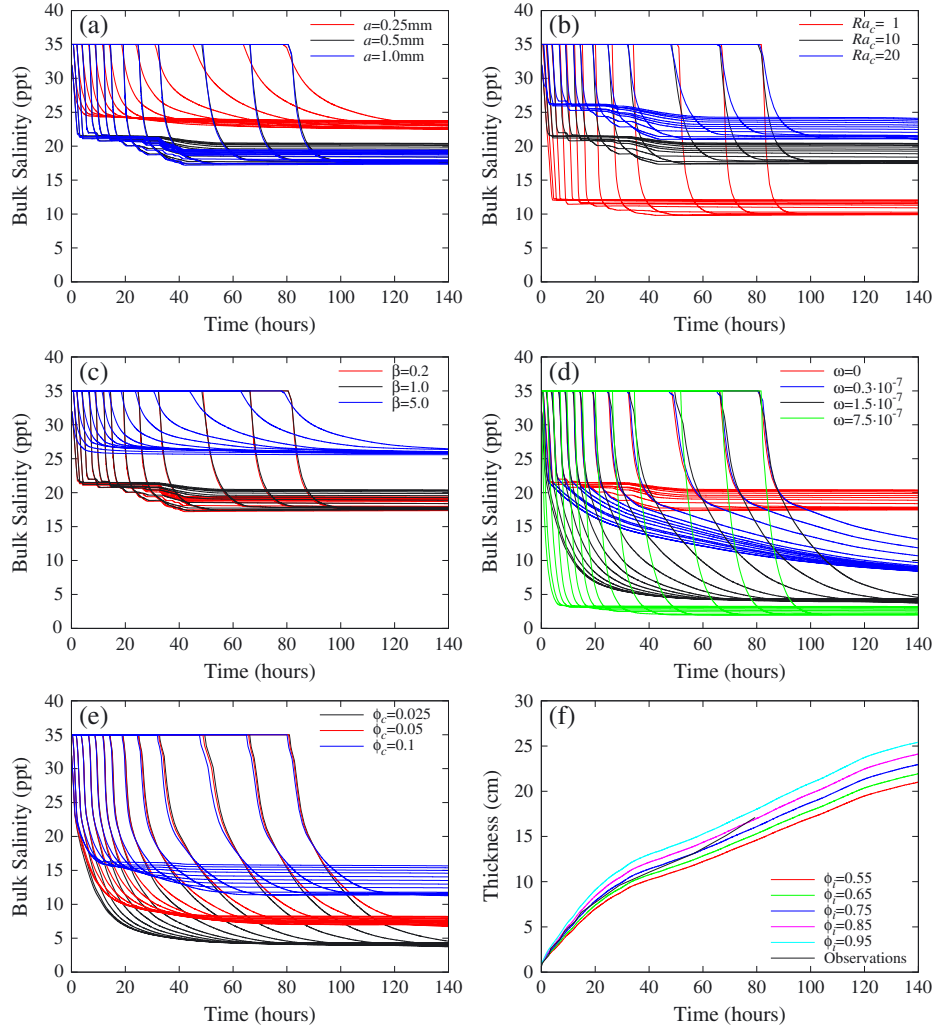


Figure 10. Sensitivity study of the adjustable parameters. Model results of bulk salinity (ppt) versus time (hours). (a) Model results for changing the channel radius, a . (b) Model results for changing the critical Rayleigh number, Ra_c . (c) Model results for changing the convection aspect ratio, β . (d) Model results for changing the slow drainage strength, ω . Note the units of ω are $\text{m s}^{-1} \text{K}^{-1}$. (e) Model results for changing the slow drainage cutoff liquid fraction, ϕ_c . (f) Ice thickness (cm) versus time (hours) for varying values of the ice-ocean interface liquid fraction, ϕ_i . Observations are shown in black. Unless otherwise stated, $a = 0.5 \text{ mm}$, $\phi_c = 0.025$, $Ra_c = 10$ and $\omega = 1.5 \times 10^{-7} \text{ m s}^{-1} \text{K}^{-1}$. $\omega = 0$ for Figures 10a–10c so that only the rapid mode of desalination is present. Both modes are present for Figures 10d–10f.

ρ_{ocn} is the ocean density, T_{ocn} is the sea surface temperature and T_{bot} is the ice bottom temperature (taken as the freezing temperature of the sea water). u_* is the friction velocity, set here to a constant value of 0.005 m/s used in CICE, since no ocean velocity measurements were available from the fieldwork site [Maykut and McPhee, 1995]. We find an ice/ocean interface solid fraction of 0.15 (the same value as that from section 4.1) reproduces the observed ice growth rate (see Figure 10f).

[49] Air temperature, relative humidity and wind speed at a height of 4 m were recorded by a weather station 4 km away from the field site. These are used in the bulk transfer formula used in CICE to calculate the upper surface fluxes. Downwelling longwave and shortwave radiation is calculated as in Hunke and Holland [2007] using ERA-interim data for total cloudiness [Dee et al., 2011], interpolated to

the geographical coordinates of Adventfjorden. We assume zero snowfall since little was observed at the fieldwork site.

[50] Figure 8 compares the modeled and observed results. Temporal evolution of temperature and bulk salinity at each of the instrumental depths is displayed. The temperature fields are reasonably reproduced, although the model results tend to have lower temperatures than observed, which may be due to inaccuracies in the downwelling longwave and shortwave fluxes. A comparison with the original CICE thermodynamics [Bitz and Lipscomb, 1999], which uses a prescribed and time independent salinity profile, show similar growth rates and ice temperatures. Currently, the Bitz and Lipscomb [1999] thermodynamic module requires around half the time to complete this simulation than does the new module, which has not yet undergone rigorous optimization for computational efficiency.

[51] The general characteristics of the bulk salinity data are also well reproduced, illustrated in Figure 9. Note that because of a saturation of the measurement electronics used for the field experiments, the salinity measurements become increasingly uncertain for very low bulk salinity values. This is because the instrument electronics have been designed to measure impedances of a certain magnitude, and impedances much higher or much lower than this range are always seen as the largest (or smallest) impedance for which the electronics were designed. The agreement between measurements and model results are usually within the measurement uncertainty, which is estimated to be up to 5 ppt. Figure 5b shows a plot of modeled bulk salinity versus observed bulk salinity. The reasonable agreement between observed and modeled bulk salinity is apparent. One issue with the model results is the lack of increased salinity near the ice surface typical of “C” shaped profiles, although the fieldwork data also seems to lack such a feature.

[52] Next we test the sensitivity of the model to changes in the tunable parameters in the two gravity-drainage parameterizations. In Figure 10a, the effect on the rapid drainage by variations in the channel diameter is explored. Only the effects of the rapid drainage are modeled. As the diameter of the channel is increased, the amount of brine drainage increases until a limiting value of the diameter is reached. Increasing the diameter further does not increase the drainage because it is limited by the Rayleigh number which becomes subcritical for bulk salinities less than ~ 20 ppt. Figures 10b and 10c show the sensitivity of the model results to the critical Rayleigh number, Ra_c , and the aspect ratio, β respectively. More desalination occurs for smaller values of both these parameters, although the amount of desalination that occurs saturates for values of the aspect ratio greater than around 1.

[53] In Figure 10d, we explore the effect on the slow drainage of changing the drainage strength. Unsurprisingly, as the strength parameter ω is increased, more drainage occurs until at high values the ice drains very rapidly to ~ 3 ppt. Figure 10e shows that lower final bulk salinities are achieved by using a smaller value of the slow drainage cutoff liquid fraction ϕ_c .

[54] The final tunable parameter in the model is the ice-ocean interface liquid fraction, ϕ_i , which controls the rate at which new congelation ice grows at the base of the ice. Increasing ϕ_i increases the rate of ice growth, as can be seen in Figure 10f, since less pure ice crystal needs to be formed for a given thickness of new mush.

5. Discussion and Conclusions

[55] The wire harp instrument described in Notz [2005], whose data we use here, affords a unique ability to explore time resolved drainage of forming sea ice. The time resolved nature of this data reveals two distinct modes of drainage: rapid drainage in a narrow region at the base of the ice and slow drainage occurring more deeply in the ice. In this paper we present a prognostic salinity parameterization suitable for inclusion in a global climate model, that reproduces both drainage modes apparent in the observed data. The rapid mode of drainage is modeled with an advective operator assuming upflow in mush and downflow through evacuated

channels. The slow drainage is modeled with a simple relaxation of the bulk salinity.

[56] The rapid drainage parameterization presented here is based on an advective operator, unlike other gravity-drainage formulations, which have generally used a diffusive parameterization. This more closely models the physical reality of gravity drainage which is thought to consist of an upward Darcy flow in the mush and downward flow through narrow channel features. Diffusion implies mixing of downward and upward flows at each level, something that is not thought to happen in gravity drainage. Our parameterization considers explicitly the pressure differences in the mush and channels that drive the flow and has only a few tunable parameters, all of which have physical meaning and whose value is approximately known.

[57] The rapid drainage parameterization also treats convection as a non-local phenomenon: values for the vertical flow velocity are calculated for an extended column in the ice. This is desirable since convection is non-local. The “local” Rayleigh number gives a measure of the strength of convection between a level in the ice and the ocean including all the intervening layers. Within a region of mush undergoing convection, there may be parts experiencing flow while having a sub-critical Rayleigh number. This is achieved when another region higher in the mush has a super critical Rayleigh number and drives the flow through a sub-critical part of the mush. The Rayleigh number goes to zero as the interface is approached from above since the Rayleigh number is proportional to the distance from the interface. Thus any parameterization that requires super-critical mush between a region interior to the ice and the ice/ocean interface will never have any gravity drainage. The parameterization of Vancoppenolle *et al.* [2010] would suffer from this problem in the limit of very fine resolution.

[58] The observations show that the slow drainage rate is only weakly a function of mush permeability and there is no apparent Rayleigh number cutoff. This mode of drainage is reasonably well fitted by a relaxation in bulk salinity and we model it as such. This is what was done by Vancoppenolle *et al.* [2009a] for all of their gravity drainage, but we use a much shorter decay lifetime. Improved metrology in future tank experiments and fieldwork studies of gravity drainage would help to identify the physical mechanism behind this slow drainage. Specifically, spatially resolved measurements of brine velocity would be helpful since this would determine whether bi-directional flow in channels, as observed by Eide and Martin [1975] and Niedrauer and Martin [1979], is significant in the drainage process.

[59] The model results lack a strong “C” shaped profile with increased salinity at the surface. This may be a problem with the parameterizations or that the conditions simulated did not result in a “C” shaped profile in reality—the fieldwork data do not show a “C” shaped profile. Other data, such as that in Weeks and Ackley [1986], show such a “C” shaped profile and future work will investigate whether this parameterization can reproduce these profiles.

[60] Drainage halts for both slow and rapid drainage modes once the ice becomes impermeable. For rapid drainage this occurs because the Rayleigh number becomes zero as the permeability goes to zero, and because the mush permeability is explicitly used to calculate the vertical flows. For slow drainage, the ice only drains until a critical

porosity for impermeability, found by *Golden et al.* [2007], is reached.

[61] In summary, the current release of the LANL sea-ice model, CICE (version 4.1), has a prescribed salinity profile for the ice and does not model the processes by which the salinity of the ice can vary. A better representation of the sea-ice hydrology is vital for modeling the ecosystem of high latitude seas, since, for example, organisms in the ice can seed oceanic plankton blooms after summer ice retreat [*Hunke et al.*, 2011]. Brine drainage also has an effect on the physical properties of the ocean: in particular the fast drainage mode could enhance deep vertical convection, while the slow drainage mode could gradually increase mixed layer salinity, eroding the halocline.

[62] Following mushy-layer theory, we have implemented and tested a new thermodynamic component for CICE featuring two-mode gravity drainage. Only the rapid drainage is controlled by the mush Rayleigh number. The new parameterization reproduces the laboratory and field experiments of *Notz* [2005] and *Notz and Worster* [2008] and demonstrates that while slow drainage occurs throughout the ice column, rapid drainage primarily affects salinities near the freezing interface. In fact, the slow drainage functions at all times in the model, but is overwhelmed by the magnitude of the rapid drainage. The model results are also reasonably insensitive to the number of vertical layers used, making the model practical for use in a global climate model. Microscale observations are essential for the further validation of this and other realistic brine drainage models; such observations are so far only sparsely available.

[63] We do not attempt to model all processes active during the sea-ice annual cycle in this paper, instead focusing on the one process that has proven most difficult to capture, gravity drainage. Other processes such as flushing, flooding and snow-ice formation are available in the new thermodynamics module and will be assessed in later publications

that include fully three-dimensional, global, hindcast simulations of sea ice. Here we demonstrate that mushy-layer theory provides a suitable modeling framework for sea-ice thermodynamics, including complex desalination processes, for large-scale sea-ice models.

Appendix A: Mushy-Layer Model

A1. Mushy-Layer Relations

[64] The mush enthalpy, q , is related to the temperature, T , and the brine volume, ϕ , by

$$q = \phi q_{\text{br}} + (1 - \phi) q_i$$

$$= \phi \rho_{\text{br}} c_{\text{br}} T + (1 - \phi)(\rho_i c_i T - \rho_i L), \quad (\text{A1})$$

where q_{br} is the brine enthalpy, q_i is the ice enthalpy, ρ_i and c_i are the density and heat capacity of the ice, ρ_{br} and c_{br} are the density and heat capacity of the brine and L is the latent heat of melting of the ice. Values used for physical properties are given in Table A1. Likewise, following equation (5), the conductivity of the mush is given by

$$K = \phi K_{\text{br}} + (1 - \phi) K_i, \quad (\text{A2})$$

where K_i is the conductivity of the ice and K_{br} is the conductivity of the brine. The thermal conductivity of brine is a function of temperature and salinity, but here we take it as a constant value equal to the value found at -10°C [*Siedler and Peters*, 1986], the middle of the temperature range experienced by sea ice. To calculate this conductivity the salinity of the brine is taken to be the liquidus salinity at -10°C .

[65] Within the parameterizations of brine drainage the brine density is a function of brine salinity [*Notz*, 2005]:

$$\rho(S_{\text{br}}) = \alpha_1 + \alpha_2 S_{\text{br}} + \alpha_3 S_{\text{br}}^2. \quad (\text{A3})$$

Outside the parameterizations of brine drainage, the densities of brine and ice are fixed at the values given in

Table A1. Physical Parameter Numerical Values

Symbol	Description	Value	Units
ρ_i	Ice density	917 ^a	kg m ⁻³
ρ_{br}	Brine density ^a	1026 ^c	kg m ⁻³
c_i	Ice heat capacity	2106 ^c	J kg ⁻¹ K ⁻¹
c_{br}	Brine heat capacity	4218 ^c	J kg ⁻¹ K ⁻¹
L	Latent heat of melting of ice	3.34×10^6 ^c	J kg ⁻¹
K_i	Heat conductivity of ice	2.3	W m ⁻¹ K ⁻¹
K_{br}	Heat conductivity of brine	0.5375	W m ⁻¹ K ⁻¹
T_0	Liquidus break temperature	-7.636	°C
a_1	High temperature liquidus slope coefficient	-18.48	g kg ⁻¹ K ⁻¹
a_2	Low temperature liquidus slope coefficient	-10.3085	g kg ⁻¹ K ⁻¹
b_1	High temperature liquidus offset coefficient	0	g kg ⁻¹
b_2	Low temperature liquidus offset coefficient	62.4	g kg ⁻¹
α_1	Constant coefficient of brine density ^b	1000.3	kg m ⁻³
α_2	Linear coefficient of brine density ^b	0.78237	kg m ⁻³ ppt ⁻¹
α_3	Quadratic coefficient of brine density ^b	2.8008×10^{-4}	kg m ⁻³ ppt ⁻²
ϕ_i	ice-ocean interface liquid fraction	0.85 ^d	-
a	Rapid drainage channel radius	0.5 ^d	mm
Ra_c	Rapid drainage critical Rayleigh number	10 ^d	-
β	Rapid drainage aspect ratio	1 ^d	-
ω	Slow drainage strength parameter	1.5×10^{-7} ^d	m s ⁻¹ K ⁻¹
ϕ_c	Slow drainage cutoff liquid fraction	0.025 ^d	-

^aFor brine density other than in the gravity-drainage parameterizations.

^bFor brine density in the gravity-drainage parameterizations.

^cStandard CICE value.

^dTunable parameter.

Table A1. The units of salinity used in the model presented in this paper are parts per thousand (ppt) whereas originally the data presented in Notz [2005] and Notz and Worster [2008] use practical salinity units (PSU). Since these two units are practically identical at the salinities considered here [Eicken, 2003], we label the observational data as ppt to avoid confusion.

A2. Liquidus Relation

[66] Assur [1958] fitted a piecewise linear relation to experimental data of Z (the ratio of mass of salt (in g) to mass of pure water (in kg) in brine) to the melting temperature: $Z = aT + b$. Salinity is the mass of salt (in g) per mass of brine (in kg) so related to Z by

$$\frac{1}{S} = \frac{1}{1000} + \frac{1}{Z}. \quad (\text{A4})$$

The data is well fitted with two linear regions,

$$S_{\text{br}} = \frac{(T + J_1)}{(T/1000 + L_1)} l_0 + \frac{(T + J_2)}{(T/1000 + L_2)} (1 - l_0), \quad (\text{A5})$$

where

$$l_0 = \begin{cases} 1 & \text{if } T \geq T_0, \\ 0 & \text{if } T < T_0 \end{cases} \quad (\text{A6})$$

$$J_{1,2} = \frac{b_{1,2}}{a_{1,2}}, \quad (\text{A7})$$

$$L_{1,2} = \frac{(1 + b_{1,2}/1000)}{a_{1,2}}. \quad (\text{A8})$$

Using this nonlinear liquidus relation allows temperature to be calculated from enthalpy by solving a quadratic equation rather than by a root finding algorithm, so maintains the numerical efficiency of a less accurate linear liquidus relation. No adverse numerical effects have been observed using this liquidus relation because of the discontinuity in gradient at T_0 .

A3. Basal Boundary Condition

[67] In traditional Stefan problems, the ice growth rate is calculated by determining the difference in heat flux on either side of the ice/ocean interface and equating this energy difference to the latent heat of new ice formed. Thus,

$$(1 - \phi_i) L \rho_i \frac{\partial h}{\partial t} = K \left. \frac{\partial T}{\partial z} \right|_i - K_w \left. \frac{\partial T}{\partial z} \right|_w, \quad (\text{A9})$$

where $(1 - \phi_i)$ is the solid fraction of new ice formed and the right hand is the difference in heat flux at the ice-ocean interface between the ice side and the ocean side of the interface. However, with mushy layers, there is usually no discontinuity in solid fraction across the interface, so $(1 - \phi_i)$ is zero and equation (A9) cannot be used explicitly. To circumvent this problem, we set the interface solid fraction to be a non-zero value (determined in sections 4.1 and 4.2 to be 0.15) that reproduces observations when the ocean temperature is near its freezing point. The basal ice temperature is set to the liquidus temperature of the ocean surface salinity.

[68] **Acknowledgments.** A.T. and E.H. are supported by the Earth System Modeling and Regional and Global Climate Modeling programs of the Office of Biological and Environmental Research within the U.S. Department of Energy's Office of Science; Los Alamos National Laboratory is operated by the National Nuclear Security Administration of the DOE under Contract DE-AC52-06NA25396. We thank Dirk Notz for the use of his data and for useful comments. We also thank Nicole Jeffery for helpful discussions and for comments on this paper.

References

- Assur, A. (1958), Composition of sea ice and its tensile strength, in *Arctic Sea Ice; Conference Held at Easton, Maryland, February 24–27, 1958*, pp. 106–138, Publishers National Research Council Washington, Washington, D. C.
- Batchelor, G. K. (1967), *An Introduction to Fluid Dynamics*, 181 pp., Cambridge University Press, Cambridge, U. K.
- Bitz, C. M., and W. H. Lipscomb (1999), An energy-conserving thermodynamic model of sea ice, *J. Geophys. Res.*, **104**, 15,669–15,677, doi: 10.1029/1999JC900100.
- Comiso, J. C. (2012), Large decadal decline of the Arctic multiyear ice cover, *J. Climate*, **25**, 1176–1193, doi:10.1175/JCLI-D-11-00113.1.
- Cox, G. F. N., and W. F. Weeks (1975), Brine drainage and initial salt entrapment in sodium chloride ice, *CRRRL Res. Rep. 345*, U.S. Army Cold Reg. Res. and Eng. Lab., Hanover, N. H.
- Cox, G. F. N., and W. F. Weeks (1988), Numerical simulations of the profile properties of undeformed first-year sea ice during the growth season, *J. Geophys. Res.*, **93**, 12,449–12,460, doi:10.1029/JC093iC10p12449.
- Dee, D. P., et al. (2011), The ERA-Interim reanalysis: Configuration and performance of the data assimilation system, *Q. J. Roy. Meteor. Soc.*, **137**, 553–597, doi:10.1002/qj.828.
- Eicken, H. (2003), From the microscopic to the macroscopic to the regional scale: Growth, microstructure and properties of sea ice, in *Sea Ice—An Introduction to its Physics, Chemistry, Biology and Geology*, edited by D. Thomas, and G. S. Dieckmann, pp. 22–81, Blackwell Science, London, U. K.
- Eide, L. I., and S. Martin (1975), The formation of brine drainage features in young sea ice, *J. Glaciol.*, **14**, 137–154.
- Feltham, D. L., N. Untersteiner, J. S. Wettlaufer, and M. G. Worster (2006), Sea ice is a mushy layer, *Geophys. Res. Lett.*, **33**, L14501, doi: 10.1029/2006GL026290.
- Freitag, J. (1999), Untersuchungen zur Hydrologie des arktischen Meeres - Konsequenzen für den kleinskaligen Stofftransport (in German), in *Ber. Polarforsch. 325*, Alfred Wegener Inst. für Polar und Meeresforsch., Bremerhaven, Germany.
- Golden, K. M., H. Eicken, A. L. Heaton, J. Miner, D. J. Pringle, and J. Zhu (2007), Thermal evolution of permeability and microstructure in sea ice, *Geophys. Res. Lett.*, **34**, L16501, doi:10.1029/2007GL030447.
- Griewank, P., and D. Notz (2011), *Modelling sea-ice desalination, poster presented at the European Geosciences Union General Assembly 2011*, Vienna, Austria.
- Hunke, E. C., and M. M. Holland (2007), Global atmospheric forcing data for Arctic ice-ocean modeling, *J. Geophys. Res.*, **112**, C04S14, doi: 10.1029/2006JC003640.
- Hunke, E. C., D. A. Notz, A. K. Turner, and M. Vancoppenolle (2011), The multiphase physics of sea ice: A review for model developers, *Cryosphere*, **5**, 989–1009, doi:10.5194/tc-5-989-2011.
- Jeffery, N., E. C. Hunke, and S. M. Elliott (2011), Modeling the transport of passive tracers in sea ice, *J. Geophys. Res.*, **116**, C07020, doi: 10.1029/2010JC006527.
- Knoll, D. A., and D. E. Keyes (2004), Jacobian-free Newton-Krylov methods: A survey of approaches and applications, *J. Comput. Phys.*, **193**, 357–397, doi:10.1016/j.jcp.2003.08.010.
- Maslanik, J. A., C. Fowler, J. Stroeve, S. Drobot, J. Zwally, D. Yi, and W. Emery (2007), A younger, thinner Arctic ice cover: Increased potential for rapid, extensive sea-ice loss, *Geophys. Res. Lett.*, **34**, L24501, doi: 10.1029/2007GL032043.
- Maus, S., and S. De La Rosa (2012), Salinity and solid fraction of frazil and grease ice, *J. Glaciol.*, **58**, 594–612, doi:10.3189/2012JoG11J110.
- Maykut, G. A., and M. G. McPhee (1995), Solar heating of the Arctic mixed layer, *J. Geophys. Res.*, **100**, 24,691–24,703, doi:10.1029/95JC02554.
- Nakawo, M., and N. K. Sinha (1981), Growth rate and salinity profile of first-year sea ice in the high arctic, *J. Glaciol.*, **27**, 315–330.
- Naumann, A. K., D. Notz, L. Håvik, and A. Sirevaag (2012), Laboratory study of initial sea-ice growth: Properties of grease ice and nilas, *Cryosphere*, **6**, 729–741, doi:10.5194/tc-6-729-2012.
- Niedrauer, T. M., and S. Martin (1979), An experimental study of brine drainage and convection in young sea ice, *J. Geophys. Res.*, **84**, 1176–1186, doi:10.1029/JC084iC03p01176.
- Nield, D. A., and A. Bejan (2006), *Convection in Porous Media*, (3rd edn), 233 pp., Springer, New York.
- Notz, D. (2005), Thermodynamic and fluid-dynamical processes in sea ice, Ph. D. thesis, University of Cambridge, Cambridge, U. K.
- Notz, D., J. S. Wettlaufer, and M. G. Worster (2005), A non-destructive method for measuring the salinity and solid fraction of growing sea ice in situ, *J. Glaciol.*, **51**(172), 159–166, doi:10.3189/172756505781829548.
- Notz, D., and M. G. Worster (2008), In situ measurements of the evolution of young sea ice, *J. Geophys. Res.*, **113**, C03001, doi: 10.1029/2007JC004333.

- Notz, D., and M. G. Worster (2009), Desalination processes of sea ice revisited, *J. Geophys. Res.*, *114*, C05006, doi:10.1029/2008JC004885.
- Phillips, O. M. (1991), *Flow and Reactions in Permeable Rocks*, 60 pp., Cambridge University Press, Cambridge, U. K.
- Siedler, G., and H. Peters (1986), Physical properties (general) of sea water, in *Landolt-Börnstein: Numerical Data and Functional Relationships in Science and Technology*, pp. 233–264, New Series / Oceanography, vol. 3a, Springer, Berlin.
- Smedsrud, L. H., and R. Skogseth (2006), Field measurements of Arctic grease ice properties and processes, *Cold Reg. Sci. Technol.*, *44*, 171–183, doi:10.1016/j.coldregions.2005.11.002.
- Untersteiner, N. (1968), Natural desalination and equilibrium salinity profile of perennial sea ice, *J. Geophys. Res.*, *73*, 1251–1257, doi:10.1029/JB073i004p01251.
- Vancoppenolle, M., C. M. Bitz, and T. Fichefet (2007), Summer landfast sea ice desalination at Point Barrow, Alaska: Modeling and observations, *J. Geophys. Res.*, *112*, C04022, doi:10.1029/2006JC003493.
- Vancoppenolle, M., T. Fichefet, H. Goosse, S. Bouillon, G. Madec, and M. A. M. Maqueda (2009a), Simulating the mass balance and salinity of Arctic and Antarctic sea ice. 1. Model description and validation, *Ocean Model.*, *27*, 33–53, doi:10.1016/j.ocemod.2008.10.005.
- Vancoppenolle, M., T. Fichefet, and H. Goosse (2009b), Simulating the mass balance and salinity of Arctic and Antarctic sea ice. 2. Importance of sea ice salinity variations, *Ocean Model.*, *27*, 54–69, doi:10.1016/j.ocemod.2008.11.003.
- Vancoppenolle, M., H. Goosse, A. de Montety, T. Fichefet, B. Tremblay, and J.-L. Tison (2010), Modeling brine and nutrient dynamics in Antarctic sea ice: The case of dissolved silica, *J. Geophys. Res.*, *115*, C02005, doi:10.1029/2009JC005369.
- Weeks, W. F., and S. F. Ackley (1986), The growth, structure and properties of sea ice, in *The Geophysics of Sea Ice. Vol. 146 of NATO ASI Series*, edited by N. Untersteiner, pp. 9–164, Plenum Press, New York and London.
- Weeks, W. F., and O. S. Lee (1958), Observations on the physical properties of sea ice at Hopedale, Labrador, *Arctic*, *11*, 134–155.
- Wells, A. J., J. S. Wettlaufer, and S. A. Orszag (2010), Maximal potential energy transport: A variational principle for solidification problems, *Phys. Rev. Lett.*, *105*, 254–502, doi:10.1103/PhysRevLett.105.254502.
- Worster, M. G. (1991), Natural convection in a mushy layer, *J. Fluid Mech.*, *224*, 335–359, doi:10.1017/S0022112091001787.
- Worster, M. G. (1992a), The dynamics of mushy layers, in *Interactive Dynamics of Convection and Solidification*, edited by S. H. Davis, et al., pp. 113–138, Kluwer Academic, Dordrecht, Netherlands.
- Worster, M. G. (1992b), Instabilities of the liquid and mushy regions during solidification of alloys, *J. Fluid Mech.*, *237*, 649–669, doi:10.1017/S0022112092003562.
- Worster, M. G. (1997), Convection in mushy layers, *Ann. Rev. Fluid Mech.*, *29*, 91–122, doi:10.1146/annurev.fluid.29.1.91.